Performance characterization of a new high resolution PET scintillation detector

# Performance characterization of a new high resolution PET scintillation detector

**A Vandenbroucke, A M K Foudray, P D Olcott and C S Levin**

Molecular Imaging Program at Stanford, Department of Radiology, Stanford, CA, USA

E-mail: arnevdb@stanford.edu and cslevin@stanford.edu

## Abstract

Performance of a new high resolution PET detection concept is presented. In this new concept, annihilation radiation enters the scintillator detectors edge-on. Each detector module comprises two $8 \times 8$ LYSO scintillator arrays of $0.91 \times 0.91 \times 1$ mm$^3$ crystals coupled to two position-sensitive avalanche photodiodes (PSAPDs) mounted on a flex circuit. Appropriate crystal segmentation allows the recording of all three spatial coordinates of the interaction(s) simultaneously with submillimeter resolution. We report an average energy resolution of $14.6 \pm 1.7\%$ for 511 keV photons at FWHM. Coincident time resolution was determined to be $2.98 \pm 0.13$ ns FWHM on average. The coincidence point spread function (PSF) has an average FWHM of $0.837 \pm 0.049$ mm (using a 500 $\mu$m spherical source) and is uniform across the arrays. Both PSF and coincident time resolution degrade when Compton interactions are included in the data. Different blurring factors were evaluated theoretically, resulting in a calculated PSF of 0.793 mm, in good agreement with the measured value.

(Some figures in this article are in colour only in the electronic version)

## 1. Introduction

Positron emission tomography (PET) is a molecular imaging modality which can detect molecular signatures of disease down to concentrations of about $10^{-11}$ to $10^{-12} \frac{\text{mol}}{L}$ (Levin 2008). The image quality in PET however is often compromised by a limited photon detection efficiency, a relatively low spatial resolution and a high background signal. As a result, current clinical whole-body systems only reliably detect tumors larger than about 7–10 mm. This relatively poor tumor detection capability causes large variability in clinical results and limits the interpretation of clinical data. For example, Avril and Adler (2007) and Wu and Gambhir (2003) reported decreased sensitivity and specificity for primary breast cancer detection for tumors smaller than 1 cm. Despite these limitations, PET already is widely used and is currently the most sensitive imaging modality to detect lymph node metastases (Avril and Adler 2007).

We propose a new scintillation detector concept, with a state-of-the-art resolution of 1 mm in all three dimensions that can be brought very close to the subject to substantially increase photon detection efficiency. We are applying this technique to build organ-specific PET cameras. In particular, we are planning to use the proposed technique in a breast-dedicated PET camera (Zhang *et al* 2007b, Lau *et al* 2008b).

Breast-dedicated PET is often referred to as positron emission mammography (PEM). Pilot studies (Schilling *et al* 2008, Tafra 2007, Berman 2007) report promising results despite the limited spatial resolution and photon sensitivity of these initial PEM instruments. The systems used in these pilot studies use relatively large crystal elements without depth of interaction (DOI) capabilities, yielding low and non-uniform spatial resolution especially in the direction orthogonal to the imaging heads (Thompson *et al* 1994, MacDonald *et al* 2008, Luo *et al* 2008). Despite these instrument limitations, the aforementioned references (Schilling *et al* 2008, Tafra 2007, Berman 2007) clearly indicate an emerging role for PEM in surgical planning and guiding biopsy. Intriguingly, these articles report on the potential for detection of ductal carcinoma *in situ* (DCIS), which is associated with early-stage breast cancer and is currently not visualized by any imaging modality. If PEM instrumentation would further be improved, PET could be helpful in breast cancer management, in terms of staging, guiding biopsy, monitoring loco-regional recurrence and assessing response to therapy.

Better PET image quality can be achieved in a number of ways. Good energy resolution distinguishes in-tissue scatter from scatter-free events. Good timing resolution reduces the non-coincident event background. These features can help to increase lesion to background contrast. Additionally, the spatial resolution could be improved by building systems with a finer detector pixel pitch and by having an instrument capable of determining the depth of interaction. The latter feature reduces the parallax error, apparent in many PET images.

A larger packing fraction yields the detection of a larger number of annihilation photons in the same field of view, resulting in higher signal to noise ratio in the PET image. In addition, the ability to bring the camera in close proximity to the breast enables increased photon sensitivity, which results in shorter scan times and/or lower dose to the patient. Therefore, patient throughput could be improved, helping to reduce the cost of the scanner.

However, the finer detector pitch and high packing fraction account for an increasing channel density and scanner complexity. Applying channel reduction techniques, such as appropriate multiplexing, decreases cost and complexity of the scanner.

This report describes the design and performance of a high resolution PET scintillation detector concept being developed in our lab. In the next section, the novel scintillation detection concept is introduced, followed by the description and results of various performance tests in the third section.

## 2. Design of a high resolution PET scintillation detector module

We are studying a high resolution PET scintillation detector concept capable of 1 mm$^3$ intrinsic spatial resolution. This section describes the new detection concept, followed by a description of the main building blocks of the system: scintillation crystal array and photo detector. Finally, a fully assembled detector module is presented.

### 2.1. Determining photon interaction points in 3D

The novel detection concept we are using has been presented before (Levin 2002), and is depicted in figure 1. A block detector is formed by stacking several module layers, each having two scintillator arrays read out by one position sensitive avalanche photodiodes (PSAPD)
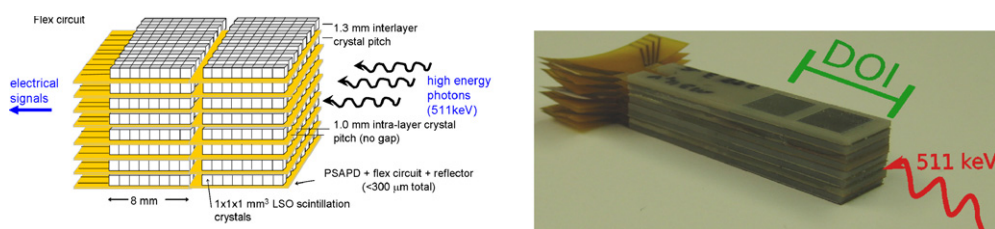
**Figure 1.** Principle of the edge-on radiation yielding three-dimensional photon positioning information.

each. Rather than converting the optical scintillation light into charge at the *back* of the block detector, we detect the scintillation light at the *sides* of the scintillation crystal elements. The annihilation photons are thus entering the module *edge-on*, rather than *face-on* in a more conventional design. This method provides multiple appealing features. First, the scintillation light collection efficiency is larger than 90% and independent of the interaction location (Levin 2002), a factor that enables excellent energy, time and spatial resolution performance. Next, the photon DOI is directly measured by the longitudinal segmentation. Third, this configuration determines all three-dimensional coordinates of each photon interaction with a sub-millimeter precision, in contrast to most other DOI designs in the literature which measure DOI coarser, and only provide essentially a low resolution single centroid for the case of multiple interactions (Lewellen 2008, Ito *et al* 2007, Inadama *et al* 2002, Seidel *et al* 1999, Moses *et al* 1995, Carrier *et al* 1988).

### 2.2. Scintillation crystal array

The requirements for a scintillation crystal for PET are high light yield, fast decay time, high density and high atomic number. Additionally, the crystal should be easily machinable so that a fine segmentation for high spatial resolution can be achieved. We choose to use lutetium yttrium orthosilicate (LYSO) which has a light output of about 27 000 optical photons per MeV of deposited energy, a 40 ns decay time and a photofraction of about 32% for 511 keV photons. The density is about $7.25 \frac{g}{cm^3}$, dependent on the amount of yttrium doping.

We choose to have crystal element dimensions of $1 \times 0.91 \times 0.91$ mm$^3$ arranged in an $8 \times 8$ array. The array segmentation is governed by a combination of the required spatial resolution, and to match the sensitive area of the PSAPD photodetector (described in the next section) used in our design. The four sides and the top surface of every individual crystal are covered with a specular reflector (VM2000 by 3M). Details on the crystal array configuration can be found in Vandenbroucke and Levin (2008).

### 2.3. Photodetector

We use PSAPDs made by RMD Inc. to convert the scintillation light into electrical charge. The position information is obtained by reading out the four corners of a resistive sheet coupled to the n-side of the avalanche photodiode. These PSAPDs have a gain of about 1000 combined with a high quantum efficiency of about 77% at 400 nm (Shah 2006). The PSAPDs need to be operated at around $-1750$ V. The active area, defined as the area for which accurate floods can be produced, is $8 \times 8$ mm$^2$ (Zhang *et al* 2007a). The PSAPD's surface measures $10 \times 10$ mm$^2$.

Since each PSAPD has five readout channels, the channel density is reduced by a factor of almost 13 ($\approx 64/5$) as opposed to a scenario where each of the 64 individual crystal are
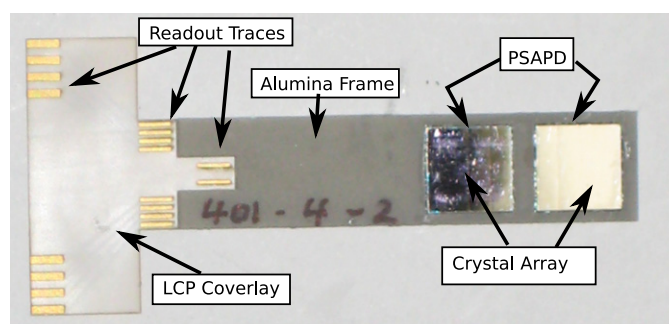
**Figure 2.** Photograph of a detector module. The flex circuit, LCP coverlay, Alumina frame and two crystal arrays are visible. The two PSAPDs are located underneath the crystal arrays of $8 \times 8$ elements, each $0.91 \times 0.91 \times 1$ mm$^3$.

attached to an array of APD devices. A dedicated multiplexing scheme explained in Lau *et al* (2008a) further reduces the number of readout channels from 10 to 6 per detector module. PSAPDs have the additional advantage of being compatible with magnetic fields, and thus these detectors can also be used in a combined PET/MR scanner.

### 2.4. Detector module

In order to achieve a high packing fraction, the PSAPD modules are mounted on a Kapton flex circuit (Zhang *et al* 2007a). The crystal arrays are precisely located in space using an alumina (Al$_2$O$_3$) frame glued to the flex circuit. Thermal simulations (Lau *et al* 2008b) showed that the thermal conductivity of alumina is sufficiently large for our project. Since moisture significantly deteriorates the performance of the PSAPD chips, the Kapton flex circuit needs to be covered with a liquid crystal polymer (LCP) coverlay to prevent moisture from leaking to the PSAPD. A photograph of a detector module is shown in figure 2, with the various components labeled on the figure. More information about the design and prototyping of this module can be found in Foudray (2008).

## 3. Testing the design

This section discusses measurements of annihilation radiation from a $^{22}$Na point source with the previously described detector module. First, data were obtained with annihilation radiation interacting *face-on* (photons entering from top of array). The face-on radiation ensures uniform radiation of all crystals in the array. By analyzing these data, we want to investigate potential systematic effects across the entire array, while having a comparable number of hits in each of the 64 crystals of the array so that data from each crystal have the same statistical power.

Next, a source was placed between two LYSO-PSAPD modules to measure *edge-on* coincidence data (photons entering the edge of the array). The detector modules will be used in this configuration in the final system. The concepts of *face-on* and *edge-on* interactions are indicated in figure 3. In the *edge-on* configuration, the front row crystals receive more hits than the subsequent rows, due to attenuation in the LYSO itself. This hinders a comparison of the performance of each individual crystal pixel and is the main reason that we investigate *face-on* data first.
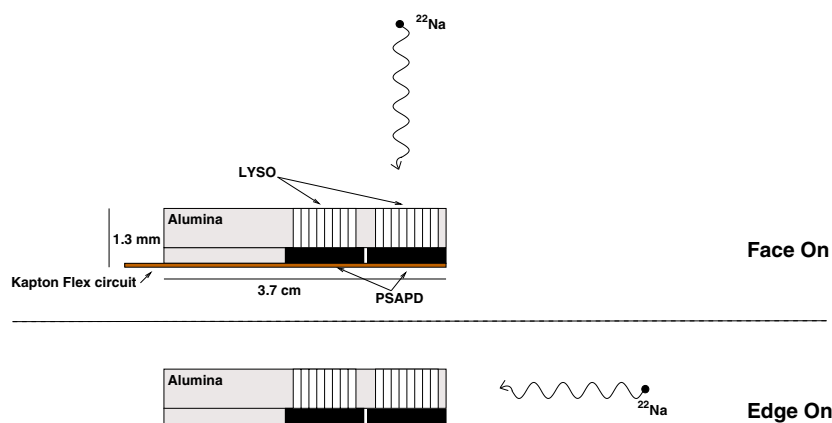
**Figure 3.** Schematic cross section of a detector module. The concepts *'face-on'* and *'edge-on'* irradiation are indicated in the figure.
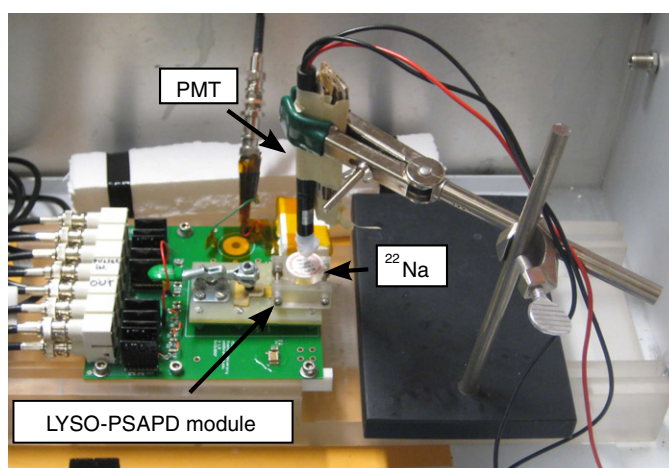


**Figure 4.** Photograph of the setup for *face-on* radiation. The $^{22}$Na source can be seen inbetween a detector module (below) and a PMT (above).

### 3.1. Face-on radiation

The first performance characterization of our detector module was done using one detector module and a *face-on* setup. To obtain timing information, a $1 \times 1 \times 1$ cm$^3$ LYSO crystal was connected to a Hamamatsu H3164 photomultiplier tube (PMT) using optical grease (BICRON BC 63) and Teflon tape. As depicted in figure 4, a $^{22}$Na point source was positioned inbetween a detector module and a PMT. The location of the source with respect to the detector module ensures face-on radiation. The vertical position of the source was adjusted to assure that the entire array is irradiated uniformly.

The PSAPD's charge output was further amplified using a charge-sensitive preamplifier (CR-110 by CREMAT). The signal from the preamplifier was fed into an ORTEC-855 spectroscopy amplifier, whose shaping time was set to 500 ns. The latter output was connected
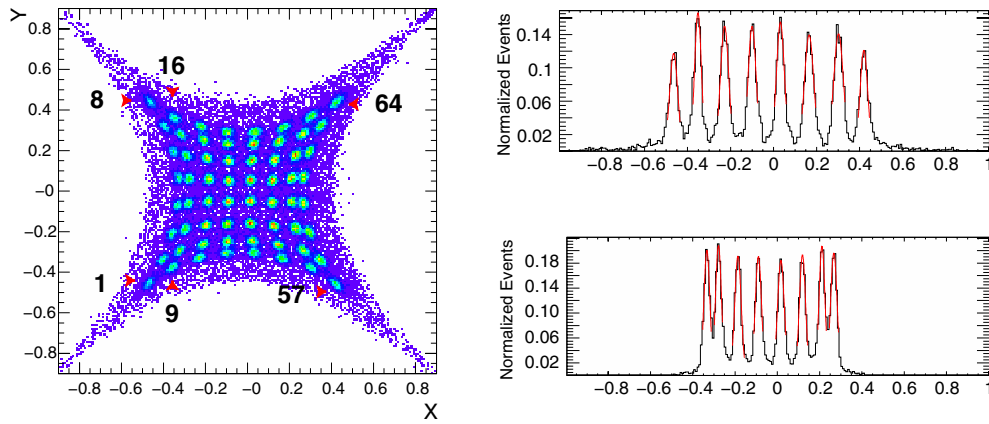
**Figure 5.** Schematic of the coincidence electronics used to read out the PSAPD and the PMT. The PSAPD's common is used for timing, its four spatial channels for energy and position information.

to an ORTEC-427A delay amplifier followed by a National Instruments ADC (NI PCI-6110). The PMT's output was amplified as well and lead into the ADC.

A schematic of the electronics used in this experiment is shown in figure 5. The timing information was obtained by the PSAPD's common signal, which was also preamplified by a CR-110 from CREMAT, and further shaped by a fast filter amplifier with an integration and differentiation time of 20 ns (ORTEC-579). An ORTEC 935 constant fraction discriminator (CFD) was used to discriminate noise and to mitigate time walk. The PMT's output was fed directly into the same CFD and served as a start signal for the ORTEC 567 time to amplitude converter (TAC). A variable fine delay between the PMT's output and the TAC accounted for calibration of the TAC. The signal of the PSAPD common served as a stop signal for the TAC. Because of the large delay used in the CFD for the PSAPD's common, no additional delay was necessary for the TAC's stop signal. The CFD threshold for both PMT and PSAPD were set well below the Compton edge and above the noise floor. One of the TAC's output went into the ADC, and the other into a gate generator (ORTEC 416A) serving as a trigger for the ADC unit.

In order to get spatial coordinates, the signals from the four corners of the resistive sheet $A$, $B$, $C$ and $D$ were combined using Anger logic in the following way:

$$
\begin{aligned}
x &= \frac{(A + B) - (C + D)}{A + B + C + D} \\
y &= \frac{(B + C) - (A + D)}{A + B + C + D}.
\end{aligned}
\tag{1}
$$

The left panel of figure 6 shows the flood histogram of one LYSO crystal array of the module. All 64 crystals are clearly identifiable. A pincushion effect is evident from the figure, which is due to nonlinearity caused by the resistive sheet in the PSAPD. A correction method for this pincushion effect has been proposed in Olcott *et al* (2005); Chaudhari *et al* (2009) and Zhang *et al* (2007c). The center and the bottom panel show a profile histogram through the corrected flood image for a top and central row, respectively. PSAPD gain decreases at the edges of the device. As a consequence, the distances between the individual crystal positions become smaller at the edges of the array, evident from the right panels in figure 6.

A crystal numbering scheme was applied so that crystal 1 is associated with the lower-left corner of the array, and the counting increases vertically up. Thus, crystal 8 corresponds

**Figure 6.** Left: a flood histogram for face-on radiation. Right top and bottom show a profile histogram for the top row and the fourth row of the linearized crystal flood histogram, respectively. The crystal numbering scheme is also indicated in the left panel.
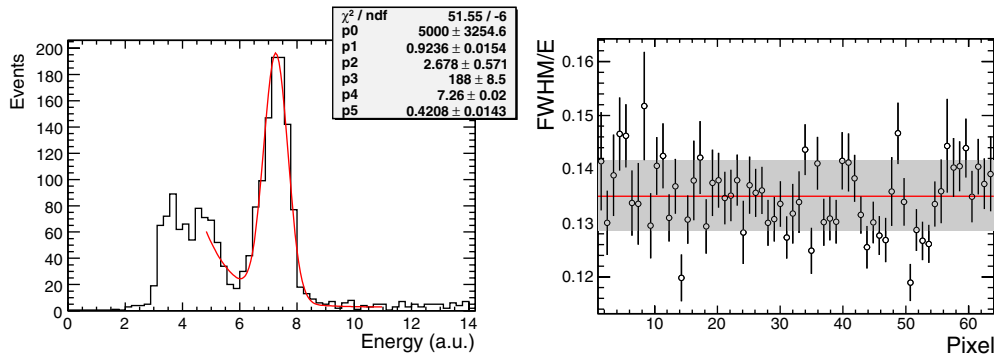


**Figure 7.** Energy spectra for one individual crystal (left) and the % energy resolution (FWHM) across the array (right). The band in the right figure indicates the RMS around the mean.

with the upper-left corner and crystal 9 is the second leftmost lower crystal. The numbering scheme is indicated in the figure as well. The 64 crystal positions were identified by a peak searching algorithm using a Markov chain as implemented in the ROOT package (Brun and Rademakers 1997). Next, these 64 peaks were geometrically ordered according to the aforementioned scheme. Each event was subsequently assigned a crystal by finding the minimum $R^2$-distance between its $(x, y)$ coordinates and the 64-position grid identified by the peak searching algorithm.

The left panel of figure 7 shows the energy spectrum for crystal number 32 of the array. The photopeak and Compton edge are clearly visible. A constant plus exponential plus Gaussian were fitted to the spectrum:

$$f(x) = p0 + e^{p1 + p2 \cdot x} + p3 \cdot e^{-\frac{1}{2}(\frac{x - p4}{p5})^2}.$$

Fit parameters are indicated in the figure. $p4$ and $p5$ correspond to the Gaussian peak position and width (sigma), respectively. An energy resolution of $13.6 \pm 0.5\%$ FWHM is obtained. The $\chi^2$ value of the fit is around 1.
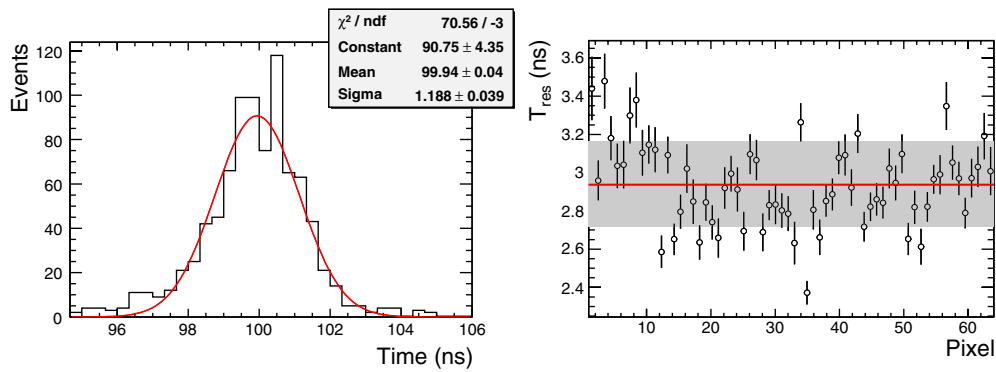
**Figure 8.** Coincident time resolution for one individual crystal (left) and the time resolution across the array (right). The band in the right figure indicates the RMS around the mean.
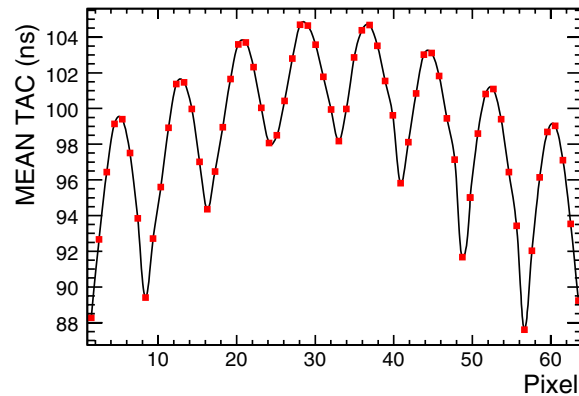


**Figure 9.** Variation of the signal arrival time across the array. The crystal pixel numbering scheme is shown in figure 6.

The variation of the energy resolution across the array is depicted in the right panel of the figure. No systematic effects can be observed. An overall average energy resolution of $13.6 \pm 0.7\%$ at FWHM is achieved.

Figure 8 shows the time resolution of the LYSO–PSAPD module in coincidence with the LYSO–PMT detector. The upper panel shows the TAC distribution for crystal number 32 of the array and the PMT. Timing is not corrected for the finite time resolution of the (slow) PMT. The right panel shows the variation of the time resolution across the array. No systematic effects can be seen and an average coincidence time resolution of $2.9 \pm 0.2$ ns FWHM is obtained. However, when looking at the signal arrival time, a clear systematic variation across the array is observed, as shown in figure 9. This variation is due to the resistive sheet coupled to the PSAPD which causes a varying $RC$-time constant across the PSAPD. A delay of about 16 ns is observed between signals coming from the middle of the PSAPD and those coming from the edge. Given the PSAPD's capacitance of about 45 pF (Dokhale *et al* 2004), the observed delay corresponds to a difference in resistance of about 0.4 $k\Omega$. The pattern is asymmetric with respect to the middle of the graph, due to the PSAPD's common contact (on top of the device) being attached to the middle of one side, thus breaking the square symmetry.
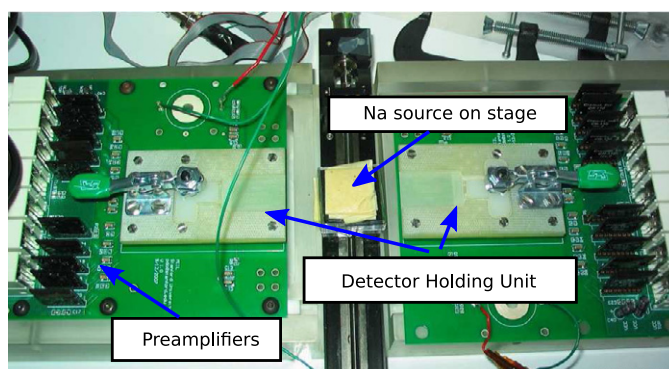
**Figure 10.** Photograph of the setup used for edge-on coincidence detection between two LYSO-PSAPD modules. Two test fixtures can be seen with a translation stage inbetween them. The CREMAT preamplifiers are visible as well. Detector modules and source are not shown in the picture.

### 3.2. Edge-on radiation

For the edge-on measurement, a 500 $\mu$m diameter spherical $^{22}$Na source was positioned on a translating stage located inbetween two LYSO–PSAPD detector module fixtures. The distance $x$ between the two modules was about 6 cm. Data were obtained in coincidence between two detector modules. The source was moved in 58 steps of 165 $\mu$m. Also, here CREMAT preamplifiers and conventional NIM electronics were used to perform pulse processing, analog as depicted in figure 5. A photograph of the edge-on setup is shown in figure 10.

Since we only had eights channels available in our ADC, the energy summation and Anger logic needed to be performed by analog processing, instead of digitally, for one module. The analog summing was performed using five ORTEC 433A dual sum and invert modules. A schematic of the NIM electronics used is depicted in figure 11.

Figure 12 shows a positioning histogram for edge-on incident radiation. As expected, a decrease in the number of hits can be seen in the lateral direction, caused by an increased distance $x$ from the source $\left(\sim\frac{1}{x^2}\right)$, and the attenuation in the LYSO crystal ($\sim$e$^{-x}$).

The energy resolution of each individual crystal in both arrays was analyzed, and an average resolution of 14.6 $\pm$ 1.7% at FWHM was obtained. The resolution is slightly worse than the one quoted for the face-on irradiation experiments. The measurements presented here were taken during a long time: in total, 64 acquisitions were acquired, each lasting about 20 min. We had no influence on the temperature inside the box. It is well established that the gain of an APD is strongly dependent on the ambient temperature as also observed in Vandenbroucke *et al* (2009). Variations in temperature may thus result in a degraded energy resolution. We do not expect this effect to be significant in the breast camera, because of the implementation of dedicated temperature regulating structures in the design (Spanoudaki *et al* 2008). Moreover, patient scan times will be shorter than the duration of the measurement presented here.

In order to investigate potential systematic interaction distribution effects, events from different combinations of opposing crystal pixel locations were analyzed. These combinations are schematically depicted in figure 13 and include coincidences between opposing rows (model A), various combinations of first and second crystals of each row (model B, C, D, and E), and a combination of a front crystal with an entire opposing row (model F and G).
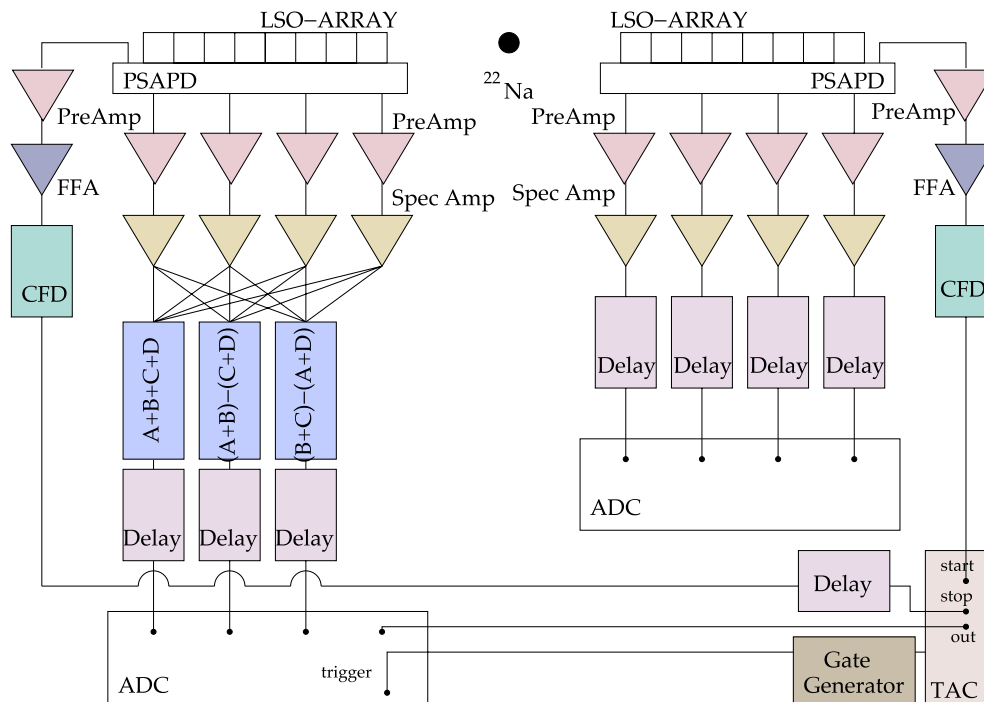
**Figure 11.** Schematic of the coincidence readout electronics used for the *edge-on* irradiation experiment. For simplicity, only three sum modules are depicted.
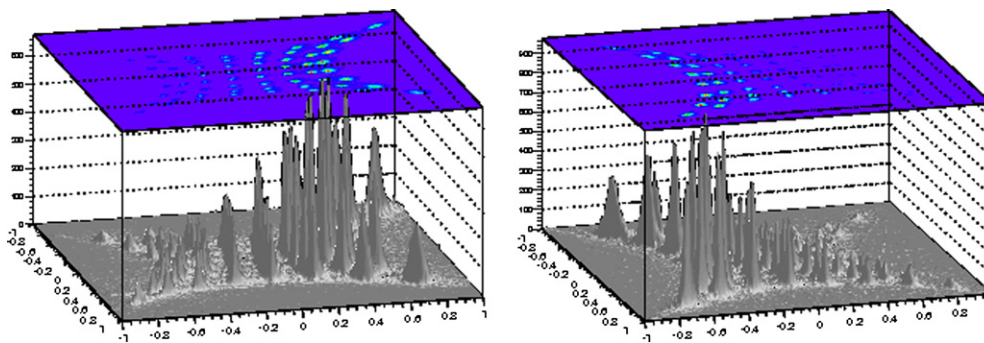


**Figure 12.** Crystal positioning histogram for both detector modules for the *edge-on* incident annihilation radiation.

The left panel of figure 14 shows the coincident time resolution for *edge-on* irradiation of two opposing rows (model A). Only eight lines of response were considered. An average time resolution of $2.98 \pm 0.13$ ns was obtained. This is similar to the face-on irradiation results. No systematic variation of the coincidence time resolution across the crystal array is observed.

For every position of the source, the number of coincidences between opposing rows were recorded. Accordingly, the so-called point spread function (PSF) is obtained, which is
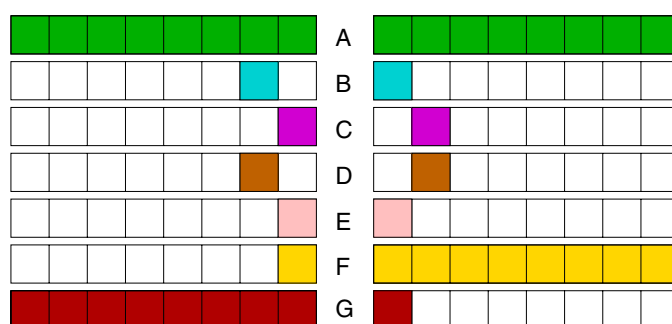
**Figure 13.** Different geometrical combinations of crystals shown in figure 15.
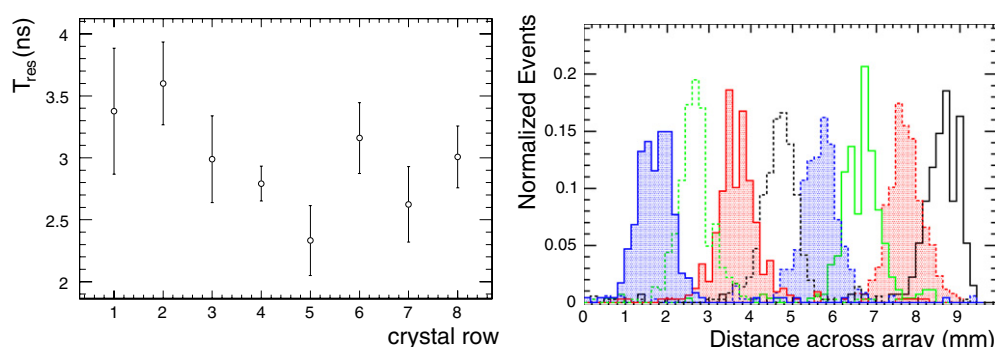


**Figure 14.** Left: coincidence time resolution of the 8 lines of response, corresponding to the combination of all crystals in opposing rows (model A in figure 13). Right: the coincidence point spread function across one edge of the array, corresponding to the number of coincidences between opposing rows (model A) for every source position. The histograms are normalized to one.

depicted on the right of figure 14. The average FWHM of the peaks is $0.837 \pm 0.045$ mm, uncorrected for the 500 $\mu$m diameter source. The measured PSF is smaller than the crystal size. From the figure it is evident that the peaks overlap below half maximum.

Figure 15 shows the coincidence time resolution at 511 keV and the point spread function for the previously mentioned geometric combinations. The different statistics are reflected in the size of the error bars. No significant deviations can be observed, aside from a slightly improved performance for model E, where coincidences between the first crystals of each row are analyzed. The PSF for that case was $0.746 \pm 0.053$ mm. Geometrically symmetric configurations like B–C and F–G had a similar coincident time resolution and a similar PSF.

As pointed out in Gu *et al* (2008) and Pratx and Levin (2009), multiple Compton interactions may add valuable information to the PET image formation process. Therefore, we analyzed the time resolution and PSF for various energy bins. Depicted in figure 16 are the global energy spectra of both opposing arrays, corrected for light yield variations across the crystal arrays and gain variations in the PSAPD. According to the figure, the 511 keV photopeak is asymmetric. This asymmetry is due to lutetium x-ray escape out of the small crystal elements. To assess the global energy resolution, a Gaussian was fit to the right tail of the photopeak, indicated by the full (blue) line in the figure. The crystal-PSAPD combination
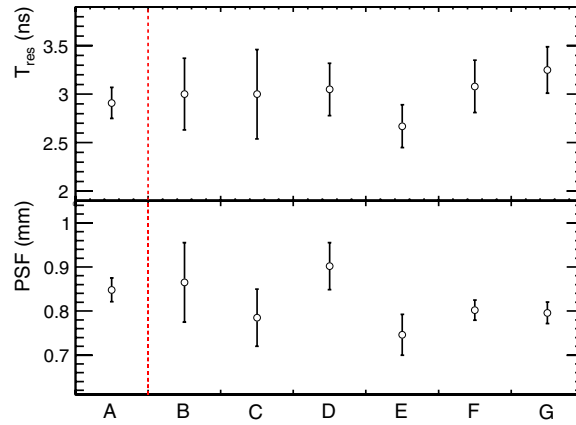
**Figure 15.** The coincidence FWHM timing resolution at 511 keV (top panel) and the point spread function (bottom panel) for different combinations of crystal pixels as indicated by figure 13 and in the text.
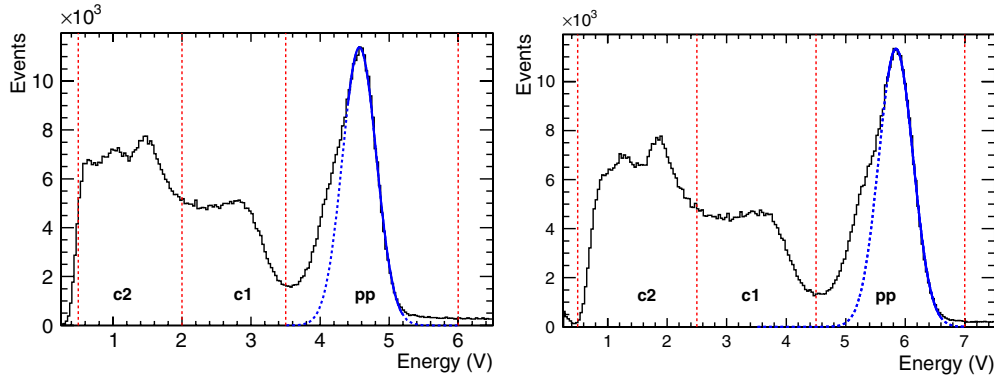


**Figure 16.** Global energy spectrum for both arrays used in the analysis. The asymmetry in the photopeak is due to x-ray escape. A Gaussian was fit to the right side of the photopeak.

in the left panel had slightly inferior energy resolution ($12.64 \pm 0.02\%$ FWHM) compared to the one on the right ($11.64 \pm 0.02\%$ FWHM). The spectrum presented in the left panel corresponds to the left module in figure 11, where for event positioning Anger logic was performed with the four analog spatial signals of the PSAPD. The energy resolutions are similar to those previously mentioned in section 3.1. The error bars stated here, however, are smaller since this is a global fit to the gain-adjusted data of all crystals, and only the upper half of the photopeak is fitted. The spectra presented in the figure were divided in three zones: a photopeak zone (pp), an upper Compton scattering zone (c1) and a lower Compton zone (c2).

In order to assess the x-ray escape energy, a double Gaussian was fit to the spectrum (not shown in the figure) using the RooFit (Verkerke and Kirkby 2003) package. When forcing both Gaussians to have the same width, an x-ray escape energy of $457.9 \pm 0.2$ keV and $455.8 \pm 0.3$ keV was obtained for the left and right spectrum, respectively. When the width of both Gaussians were allowed to be different, $456.0 \pm 0.8$ keV and $459.7 \pm 0.6$ was obtained. According to Mehta *et al* (1987), the $K\alpha_1$ x-ray (corresponding to $L_3 \rightarrow K$ transitions) is at 56 keV for $^{177}_{71}Lu$, and has a relative probability of about 50%, and the $K\alpha_2$ x-ray at 55 keV
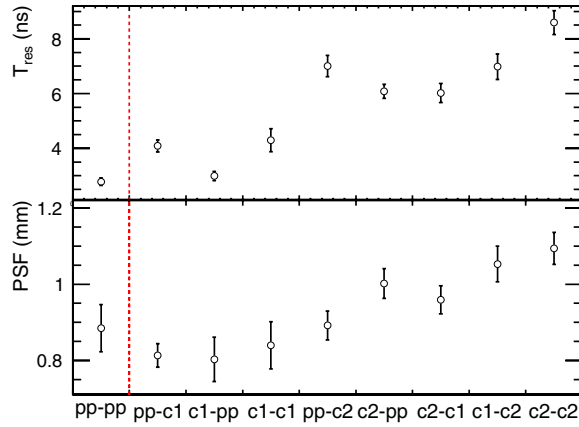
**Figure 17.** The coincidence FWHM timing resolution at 511 keV (top panel) and the point spread function (bottom panel) for different combinations of energy windows.

$(L_2 \rightarrow K)$, has a probability of about 29%. The $K\beta_{1,3}$ and $K\beta_2$ ($M \rightarrow K$) at 63 keV and 65 keV, respectively, have probabilities of about 16% and 4%. Therefore, we expect a dominant x-ray escape peak at around 454 keV, in good agreement with the fit results.

Figure 17 shows the coincidence time resolution and the PSF for the different combinations of detector energy windows illustrated in figure 16. Clearly, the time resolution degrades when Compton interactions are included. The PSF shows a similar degradation pattern when Compton interactions are included in the analysis.

The time resolution decrease can be explained by its dependence on signal amplitude and slope (Leo 1994):

$$t_{res} = \frac{\sigma_{n,1}}{\left| \frac{dV_1}{dt} \right|} \otimes \frac{\sigma_{n,2}}{\left| \frac{dV_2}{dt} \right|}, \tag{2}$$

where $\sigma_{n,(1,2)}$ is the standard deviation in amplitude $V_{(1,2)}$ due to noise and statistics for detectors 1 and detector 2, respectively. Compton interactions have lower energy deposited in the crystal array compared to photoelectric interactions. Since optical light creation in the scintillator is a Poisson process, the variance will be relatively larger for smaller energy deposition. Also, the slope of the PSAPD signal is smaller for smaller signals. These combined effects cause the degraded time resolution observed for events that use lower energy windows.

In order to investigate the degraded PSF for Compton events, the *edge-on* positioning histograms for the three different energy zones are depicted in figure 18. A profound degradation in crystal identification is observed. Individual crystals in the left histogram appear as sharp dots, whereas in the rightmost histogram, these crystals are significantly blurred. The reason for this smearing can be found in the Poisson nature of the scintillation process combined with the arithmetic of the Anger logic from equation (1).

The PSF describes the response of an imaging system to a point source or point object. Theoretically, we would expect a triangular response function with FWHM half the pixel size, in our case 455 $\mu$m. The triangular response is a convolution of two rectangular functions each one corresponding to one pixel. Assuming that both 511 keV photons are about 180° degrees apart, the FWHM of the triangular function is only half the pixel size. In our experimental setup, the object being imaged is not quite a point source. First, we used a 500 $\mu$m diameter source. Additional blurring is caused by the kinetic energy of the emitted positron, referred
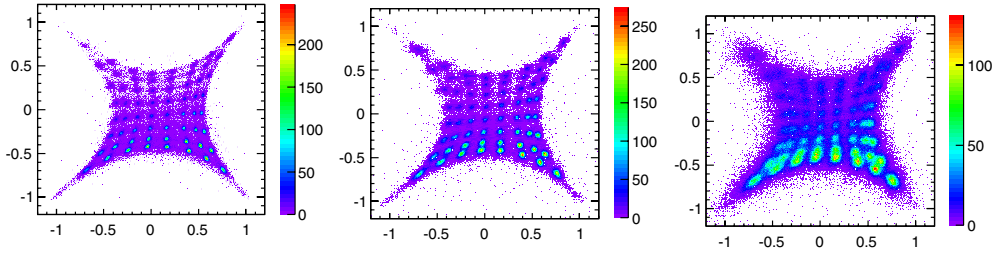
**Figure 18.** *Edge-on* irradiation positioning histogram for different energy windows. Left/middle/right correspond to zones pp/c1/c2 for the module depicted in the right panel of figure 16. See figure 12 for *edge-on* irradiation geometry.

**Table 1.** Analytical description of the blurring factors in the observed PSF.

| | Formula | Parameters |
|---|---|---|
| Positron range | $\mathbf{R} = C \cdot e^{-k_1 x} + (1 - C) \cdot e^{-k_2 x}$ | $C = 0.520, k_1 = 30.5, k_2 = 3.44$ |
| Acolinearity | $\mathbf{A} = e^{-\frac{x^2}{2\sigma^2}}$ | $\sigma = 0.00243 \cdot D/2.35 (D = 60\,\text{mm})$ |
| Source width | $\mathbf{S} = R^2 - x^2$ | $R = 250\,\mu\text{m}$ |
| Response function | $\mathbf{T} = \text{rect}(a/2) \otimes \text{rect}(a/2)$ | $a = 455\,\mu\text{m}$ |

to as 'positron range'. Thirdly, due to the residual kinetic energy of the electron–positron pair in the lab frame upon annihilation, the emitted photons are not exactly 180° apart.

The observed PSF thus is a convolution of the aforementioned blurring factors:

$$PSF = \mathbf{R} \otimes \mathbf{A} \otimes \mathbf{S} \otimes \mathbf{T}, \tag{3}$$

where $\mathbf{R}$ is the positron range, $\mathbf{A}$ is the acolinearity, $\mathbf{S}$ is the source width and $\mathbf{T}$ is the detector response. Analytical formulas of these functions are given in table 1. $\mathbf{R}$ is a cusp-like function taken from Levin and Hoffman (1999) and Haber *et al* (1990). Unfortunately, Levin and Hoffman (1999) and Haber *et al* (1990) only give parameters for $^{18}$F, $^{11}$C, $^{13}$N and $^{15}$O. The end point energy for positrons coming from $^{18}$F decay is 632 keV as opposed to 546 keV for $^{22}$Na. In order to cope with this $\sim 15\%$ difference, the code from Levin and Hoffman (1999) was adjusted to incorporate $^{22}$Na. The parameters are mentioned in table 1.

$\mathbf{A}$ is well described by a Gaussian distribution with FWHM $= 2.35\sigma = 0.0024 \cdot D$ (Shibuya *et al* 2007), where D is the distance between the two detectors. Detailed measurements of the acolinearity in Shibuya *et al* (2007) yielded a blurring of $0.0024 \cdot D$ rather than the more commonly used $0.0022 \cdot D$ from Derenzo *et al* (1993).

$\mathbf{S}$ was estimated by a double integral of a sphere. According to Gutierrez (2009) the activity is uniform across the sphere. Therefore, a weight function of 1 is used when calculating the projection of the sphere onto a line:

$$\mathbf{S} = \int_{-\sqrt{R^2-x^2}}^{\sqrt{R^2-x^2}} dy \int_{-\sqrt{R^2-(x^2+y^2)}}^{\sqrt{R^2-(x^2+y^2)}} dz \tag{4}$$

$$= \pi \cdot (R^2 - x^2). \tag{5}$$

$\mathbf{T}$ is the convolution of two rectangular functions. Because of the constraint that both photons are emitted back to back, a triangular function with FWHM equal to half the crystal size is obtained.
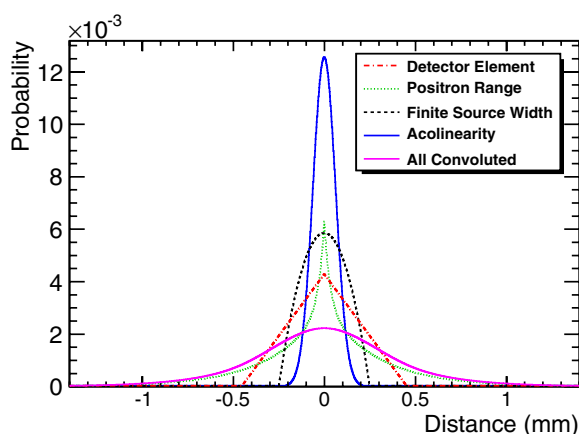
**Figure 19.** Four blurring contributions to the observed PSF. The convolution of those four functions is plotted as well. All distributions are normalized to have a unity integral.

Figure 19 shows the different contributions together with the convolution of all those blurring functions. The convolution was calculated in the Fourier space using the FFTW package (Frigo and Johnson 2005). The resulting distribution was fit with the sum of three Gaussian functions. The overall FWHM of these three Gaussians was 793 $\mu$m, which is in good agreement with the measured value of $0.837 \pm 0.045$ mm.

The good agreement between calculated and measured PSF also shows that the so-called block-effect blurring is minimal. This block-effect is often introduced to match experimental data with calculations (Derenzo *et al* 1993, Stickel and Cherry 2005, Moses and Derenzo 1993, Tomic *et al* 2005) and is caused by the light sharing in conventional block detectors. In our design, we do not have significant light sharing but only have *charge* sharing in the PSAPD.

## 4. Summary and conclusions

We are studying a high resolution PET scintillation detector concept capable of depth of interaction measurement as well as positioning the 3D coordinates of individual photon multiple interactions in the scintillator with submillimeter resolution in all three dimensions. In this new detector orientation, annihilation photons interact with the detector *edge-on*. Detector modules are built out of LYSO crystal arrays coupled to PSAPDs mounted on a flex circuit.

We presented tests of those detector modules for both *face-on* and *edge-on* radiation. The *face-on* measurements yielded an energy resolution of $13.5 \pm 0.7\%$ FWHM and a coincident time resolution of $2.9 \pm 0.2$ ns FWHM and showed no systematic variations across the array. The *edge-on* data yielded an average energy resolution of $14.6 \pm 1.7\%$ FWHM, and an average time resolution of $2.98 \pm 0.13$ ns. The point spread function indicated a spatial resolution of $0.837 \pm 0.045$ mm, in agreement with analytical calculations. Both PSF and coincident time resolution are impaired when Compton interactions are included in the analysis. Interestingly, the PSF remains below 1 mm when only one side has Compton events. A theoretical assessment of all blurring factors yielded a predicted PSF of 793 $\mu$m, in good agreement with the experimental result, indicating that the so-called block effect blurring is minimal in our design.

This report verifies the proof of principle of our high resolution 3D positioning PET detectors. The data presented here show the functionality of the basic building blocks of this new detector concept. Tests are under way with detector blocks built out of several layers of detector modules. We are currently developing a breast dedicated PET scanner using the presented modules. More details about this breast dedicated system can be found in Lau *et al* (2008b); Zhang *et al* (2007a) and Spanoudaki *et al* (2008). We also plan to build a small animal imaging system with these modules.

## Acknowledgments

## References

Avril N and Adler L 2007 F-18 Fluorodeoxyglucose-positron emission tomography imaging for primary breast cancer and loco-regional staging *Radiol. Clin. N Am* **45** 645–57

Berman C G 2007 Recent advances in breast-specific imaging *Cancer Control* **14** 338–49

Brun R and Rademakers F 1997 ROOT: an object oriented data analysis framework *Nucl. Instrum. Meth.* A **389** 81–6

Carrier C, Martel C, Schmitt D and Lecomte R 1988 Design of a high resolution positron emission tomograph using solid state scintillation detectors *IEEE Trans. Nucl. Sci.* **35** 685–90

Chaudhari A, Joshi A, Wu Y, Leahy R, Cherry S and Badawi R 2009 Spatial distortion correction and crystal identification for MRI-compatible position-sensitive avalanche photodiode based PET scanners *IEEE Trans. Nucl. Sci.* **56** 549–56

Derenzo S E, Moses W W, Huesman R H and Budinger T F 1993 Critical instrumentation issues for <2 mm resolution, high sensitivity brain PET *Quantification of Brain Function* (Amsterdam: Elsevier) pp 25–37

Dokhale P, Silverman R, Shah K, Grazioso R, Farrell R, Glodo J, McClish M, Entine G, Tran V H and Cherry S 2004 Performance measurements of a depth-encoding PET detector module based on position-sensitive avalanche photodiode read-out *Phys. Med. Biol.* **49** 4291–304

Foudray A 2008 Design of an advanced positron emission tomography detector system and algorithms for imaging small animal models of human disease *Phd Thesis* University of California, San Diego

Frigo M and Johnson S G 2005 The design and implementation of FFTW3 *Proc. IEEE* vol 93 pp 216–31

Gu Y, Pratx G, Lau F W Y and Levin C S 2008 Effects of multiple photon interactions in a high resolution PET system that uses 3-D positioning detectors *IEEE Nuclear Science Symp. Conf. Rec.* pp 3814–9

Gutierrez D 2009 Eckert & Ziegler Strahlen- und Medizintechnik AG (private communication)

Haber S F, Derenzo S E and Uber D 1990 Application of mathematical removal of positron range blurring in positron emission tomography *IEEE Trans. Nucl. Sci.* **37** 1293–9

Inadama N, Murayama H, Omura T, Yamashita T, Yamamoto S, Ishibashi H, Kawai H, Omi K, Umehara T and Kasahara T 2002 A depth of interaction detector for PET with GSO crystals doped with different amounts of Ce *IEEE Trans. Nucl. Sci.* **49** 629–33

Ito M *et al* 2007 Four-layer DOI detector with a relative offset in animal PET system *IEEE Nuclear Science Symp. Conf. Rec.* **6** 4296–9

Lau F W, Vandenbroucke A, Reynolds P D, Olcott P D, Horowitz M A and Levin C S 2008 Front-end electronics for a 1 mm$^3$ resolution avalanche photodiode based PET system with analog signal multiplexing *IEEE Nuclear Science Symp. Conf. Rec.* pp 3871–4

Lau F W Y, Fang C, Reynolds P D, Olcott P D, Vandenbroucke A, Spanoudaki V C, Olutade F, Horowitz M A and Levin C S 2008 1 mm$^3$ resolution breast-dedicated PET system *IEEE Nuclear Science Symp. Conf. Rec.* pp 5619–22

Leo W R 1994 *Techniques for Nuclear and Particle Physics Experiments* 2nd edn (Berlin: Springer)

Levin C S 2002 Design of a high-resolution and high-sensitivity scintillation crystal array for PET with nearly complete light collection *IEEE Trans. Nucl. Sci.* **49** 2236–43

Levin C S 2008 New imaging technologies to enhance the molecular sensitivity of positron emission tomography *IEEE Nuclear Science Symp. Conf. Rec.* **96** 439–67

Levin C S and Hoffman E J 1999 Calculation of positron range and its effect on the fundamental limit of positron emission tomography system spatial resolution *Phys. Med. Biol.* **44** 781–99

Levin C S and Hoffman E J 2000 Calculation of positron range and its effect on the fundamental limit of positron emission tomography system spatial resolution *Phys. Med. Biol.* **45** 559 (erratum)

Lewellen T K 2008 Recent developments in PET detector technology *Phys. Med. Biol.* **53** R287

Luo W, Anashkin E and Matthews C G 2008 First test results of a commercially available clinical PET scanner using the NEMA NU4-2008 small animal PET standards *IEEE Nuclear Science Symp. Conf. Rec.* pp 4718–23

MacDonald L E, Edwards J, Lewellen T, Haseley D, Rogers J and Kinahan P 2008 Clinical imaging characteristics of the positron emission mammography PEM Flex Solo II *IEEE Nuclear Science Symp. Conf. Rec.* pp 4494–501

Mehta D, Chand B, Singh S, Garg M, Singh N, Cheema T and Trehan P 1987 X-ray and gamma-ray intensity measurements in $^{210}$Pb, $^{177}$Lu, $^{170}$Tm and $^{141}$Ce decays *Nucl. Instrum. Methods Phys. Res.* **260** 157–9

Moses W, Derenzo S, Melcher C and Manente R 1995 A room temperature LSO/PIN photodiode PET detector module that measures depth of interaction *IEEE Trans. Nucl. Sci.* **42** 1085–9

Moses W W and Derenzo S E 1993 Empirical observation of resolution degradation in positron emission tomographs utilizing block detectors *J. Nucl. Med.* **34** 101

Tomic N, Thompson C J and Casey M E 2005 Investigation of the 'block effect' on spatial resolution in PET detectors *IEEE Trans. Nucl. Sci.* **52** 599–605

Olcott P D, Zhang J, Levin C S, Habte F and Foudray A M K 2005 Finite element model based spatial linearity correction for scintillation detectors that use position sensitive avalanche photodiodes *IEEE Nuclear Science Symp. Conf. Rec.* **5** 2459–62

Pratx G and Levin C S 2009 Bayesian reconstruction of photon interaction sequences for high-resolution PET detectors *Phys. Med. Biol.* **54** 5073–94

Schilling K, Conti P, Adler L and Tafra L 2008 The role of positron emission mammography in breast cancer imaging and management *Appl. Radiol.* **34** 26–36

Seidel J, Vaquero J, Siegel S, Gandler W and Green M 1999 Depth identification accuracy of a three layer phoswich PET detector module *IEEE Trans. Nucl. Sci.* **46** 485–90

Shah K 2006 A novel position sensitive detector for nuclear radiation. Final report to the Department of Energy, RMD, Inc., Watertown, MA

Shibuya K, Yoshida E, Nishikido F, Suzuki T, Tsuda T, Inadama N, Yamay T and Murayama H 2007 Annihilation photon acollinearity in PET: volunteer and phantom FDG studies *Phys. Med. Biol.* **52** 5249–61

Spanoudaki V C, Vandenbroucke A, Lau F W Y, Fang C and Levin C S 2008 Effects of thermal regulation structures on the photon sensitivity and spatial resolution of a 1 mm$^3$ resolution breast-dedicated PET system *IEEE Nuclear Science Symp. Conf. Rec.* pp 5657–61

Stickel J R and Cherry S R 2005 High-resolution PET detector design: modelling components of intrinsic resolution *Phys. Med. Biol.* **50** 179–95

Tafra L 2007 Positron emission tomography (PET) and mammography (PEM) for breast cancer: importance to surgeons *Ann. Surg. Oncol.* **14** 3–13

Thompson C J, Murthy K, Weinberg I N and Mako F 1994 Feasibility study for positron emission mammography *Med. Phys.* **21** 529–38

Vandenbroucke A, Lee J, Spanoudaki V, Lau F W Y, Reynolds P and Levin C 2009 Temperature and bias voltage studies of a large area position sensitive avalanche photodiode *IEEE Nuclear Science Symp. Conf. Rec.* pp 3664–9

Vandenbroucke A and Levin C S 2008 Array parameters for an advanced PET scanner dedicated to breast cancer imaging *IEEE Nuclear Science Symp. Conf. Rec.* pp 4914–9

Verkerke W and Kirkby D 2003 The RooFit toolkit for data modeling *Proc. Conf. for Computing in High-Energy and Nuclear Physics (CHEP 03)* arXiv:physics/0306116v1

Wu D and Gambhir S 2003 Positron emission tomography in diagnostive and management of invasive breast cancer: current status and future perspectives *Clin Breast Cancer* **4** S55–63

Zhang J, Foudray A, Olcott P, Farrell R, Shah K and Levin C 2007 Performance characterization of a novel thin position-sensitive avalanche photodiode for 1 mm resolution positron emission tomography *IEEE Trans. Nucl. Sci.* **54** 415–21

Zhang J, Olcott P D, Chinn G, Foudray A M K and Levin C S 2007 Study of the performance of a novel 1 mm resolution dual-panel PET camera design dedicated to breast cancer imaging using Monte Carlo simulation *Med. Phys.* **34** 689–702

Zhang J, Olcott P D and Levin C S 2007 A new positioning algorithm for position-sensitive avalanche photodiodes *IEEE Trans. Nucl. Sci.* **54** 433–7